

Article

Schottky Junctions with Bi@Bi₂MoO₆ Core-Shell Photocatalysts toward High-Efficiency Solar N₂-to-Ammonia Conversion in Aqueous Phase

Meijiao Wang¹, Guosong Wei¹, Renjie Li¹, Meng Yu¹, Guangbo Liu^{2,*} and Yanhua Peng^{1,*}

¹ College of Chemistry and Chemical Engineering, Qingdao University, Qingdao 266071, China; 15753740944@163.com (M.W.); 18563620407@163.com (G.W.); lrj222629@163.com (R.L.); yumeng1@qdu.edu.cn (M.Y.)

² Key Laboratory of Biofuels, Qingdao Institute of Bioenergy and Bioprocess Technology, Chinese Academy of Sciences, Qingdao 266101, China

* Correspondence: liugb@qibebt.ac.cn (G.L.); yhpeng@qdu.edu.cn (Y.P.)

Abstract: The photocatalytic nitrogen reduction reaction (NRR) in aqueous solution is a green and sustainable strategy for ammonia production. Nonetheless, the efficiency of the process still has a wide gap compared to that of the Haber–Bosch one due to the difficulty of N₂ activation and the quick recombination of photo-generated carriers. Herein, a core-shell Bi@Bi₂MoO₆ microsphere through constructing Schottky junctions has been explored as a robust photocatalyst toward N₂ reduction to NH₃. Metal Bi self-reduced onto Bi₂MoO₆ not only spurs the photo-generated electron and hole separation owing to the Schottky junction at the interface of Bi and Bi₂MoO₆ but also promotes N₂ adsorption and activation at Bi active sites synchronously. As a result, the yield of the photocatalytic N₂-to-ammonia conversion reaches up to 173.40 μmol g⁻¹ on core-shell Bi@Bi₂MoO₆ photocatalysts, as much as two times of that of bare Bi₂MoO₆. This work provides a new design for the decarbonization of the nitrogen reduction reaction by the utilization of renewable energy sources.

Keywords: nitrogen reduction reaction; Schottky junction; core-shell structure; localized surface plasmon resonance; Bi@Bi₂MoO₆



Citation: Wang, M.; Wei, G.; Li, R.; Yu, M.; Liu, G.; Peng, Y. Schottky Junctions with Bi@Bi₂MoO₆ Core-Shell Photocatalysts toward High-Efficiency Solar N₂-to-Ammonia Conversion in Aqueous Phase. *Nanomaterials* **2024**, *14*, 780. <https://doi.org/10.3390/nano14090780>

Academic Editor: Detlef W. Bahnemann

Received: 9 April 2024
Revised: 27 April 2024
Accepted: 29 April 2024
Published: 30 April 2024



Copyright: © 2024 by the authors. Licensee MDPI, Basel, Switzerland. This article is an open access article distributed under the terms and conditions of the Creative Commons Attribution (CC BY) license (<https://creativecommons.org/licenses/by/4.0/>).

1. Introduction

Ammonia (NH₃) is one of the most essential fundamental industrial chemicals owing to its roles in carbon-free energy storage and the production of fertilizer [1–3]. The Haber–Bosch process for industrial synthetic ammonia requires greatly harsh conditions operating at a very high temperature (≈700 K) and very high pressures (≈100 atm), which result in great energy consumption and environment-harmful gas emissions [4–6]. Compared to the conventional process, the photocatalytic nitrogen reduction reaction (NRR) in aqueous solution offers a green and sustainable technology for ammonia production, which promotes widespread investigations [7–10]. However, the efficiency of this process still has a wide gap compared to that of the Haber–Bosch one due to the difficulty of N₂ activation and the quick recombination of photo-generated carriers [11–13]. The strategies of innovative fabrication for functional material design, including defect and dopant engineering, heterojunction construction by integrating a semiconductor and metal or another semiconductor, reactive crystal facet exposure and so on, have been widely explored [14–17]. The purpose mainly focuses on the functionality that not only facilitates the separation of photo-excited electrons and holes but also provides more N₂ activation sites for solar-to-ammonia conversion.

Among numerous photocatalysts, bismuth molybdate (Bi₂MoO₆) has been widely employed for photocatalytic nitrogen fixation due to the low cost, environmentally friendly characteristics, excellent thermal and chemical stability and tunable physical and electronic properties [18,19]. As the simplest member of the Aurivillius oxide family, Bi₂MoO₆

possesses a fascinating structure that is composed of $[\text{Bi}_2\text{O}_2]^{2+}$ slices linking with a corner-sharing structure of MoO_6 octahedra [20]. The layered configuration decides the visible light response and facilitates good electron conductivity. However, Bi_2MoO_6 also faces the same problems as all photocatalysts that are the sluggish transportation and the rapid recombination of photo-generated carriers, which leads to the low photocatalytic efficiency for the NRR. The formation of a Schottky junction by rectifying contact between semiconductors and metals can facilitate the separation of photo-generated carriers and trap the electrons on metals due to the low-lying Fermi level (E_F) [21,22]. Thus, tremendous efforts have been devoted to suppressing external electron–hole recombination and maximizing the utilization of incident photons. Some noble metals (Au, Ag, etc.) loading on the Bi_2MoO_6 surface to form Schottky barriers and excite the localized surface plasmon resonance (LSPR) synchronously has been proven to be an efficient strategy [23–27]. However, the Schottky junctions' directed charge transfer results in the depletion of electrons at Bi_2MoO_6 , which is disadvantageous for N_2 adsorption and activation dominated by electron transfer. In addition, loaded noble metals always become the active centers for concomitant H_2 production due to the weak metal hydrogen strength, thereby suppressing the NRR.

Metal bismuth (Bi) is an ideal choice to take the place of noble metals due to its lower cost and strong plasmonic effect [28–30]. Most importantly, Bi can be easily self-reduced onto Bi_2MoO_6 by an in situ solvothermal process with its unique advantages of the intimate interfacial contact between Bi and Bi_2MoO_6 due to the same containing elements [31–33]. Theoretical studies by Norskov and coworkers reported the low HER activity of Bi due to the highest hydrogen binding energy (~ 0.75 eV) [34]. Moreover, it is found that N_2 preferably adsorbs at Bi sites with an end-on bound structure, which suggests favorable N_2 adsorption and activation at Bi sites [35,36]. Recently, many investigations have proved that Bi/semiconductors possess obviously enhanced photocatalytic activity in the NRR [37,38]. Huang et al. deposited Bi nanoparticles on BiOBr to construct a Schottky junction and found greatly improved photocatalytic NRR performance in an aqueous reaction [22]. However, the Schottky junction has a limited interface contact as compared with the core-shell structure. In our previous studies, it was found that the formation of core-shell heterojunctions makes obviously enhanced photocatalytic activity [39–41]. Therefore, the core-shell $\text{Bi}@\text{Bi}_2\text{MoO}_6$ Schottky junction on a highly efficient photocatalytic NRR can be expected.

Herein, a core-shell $\text{Bi}@\text{Bi}_2\text{MoO}_6$ microsphere through constructing Schottky junctions is explored as a robust photocatalyst toward N_2 reduction to ammonia. Metal Bi self-reduced onto Bi_2MoO_6 not only spurs the photo-generated electron and hole separation owing to the Schottky junction at the interface of Bi and Bi_2MoO_6 but also promotes N_2 adsorption and activation at Bi active sites synchronously. As a result, the yield of the photocatalytic N_2 -to-ammonia conversion reaches up to $173.40 \mu\text{mol g}^{-1}$ on core-shell $\text{Bi}@\text{Bi}_2\text{MoO}_6$ photocatalysts, as much as two times of that of bare Bi_2MoO_6 .

2. Experimental Section

2.1. Materials

All of the chemical reagents involving bismuth nitrate pentahydrate ($\text{Bi}(\text{NO}_3)_3 \cdot 5\text{H}_2\text{O}$), sodium molybdate dihydrate ($\text{Na}_2\text{MoO}_4 \cdot 2\text{H}_2\text{O}$), ethylene glycol (EG), ethanol absolute ($\text{C}_2\text{H}_5\text{OH}$), sodium hydroxide (NaOH) and ammonium chloride (NH_4Cl) are of analytical grade without any additional purification.

2.2. Preparation of Photocatalysts

Synthesis of Bi_2MoO_6 : Bi_2MoO_6 microspheres were prepared by a simple solvothermal method [24]. Typically, 2.0 mmol of $\text{Bi}(\text{NO}_3)_3 \cdot 5\text{H}_2\text{O}$ and 1.0 mmol of $\text{Na}_2\text{MoO}_4 \cdot 2\text{H}_2\text{O}$ were dissolved in 30 mL of ethylene glycol (EG), respectively. Then, the mixture was stirred vigorously until a clear solution was formed. Subsequently, the sodium molybdate solution was slowly dripped into the bismuth nitrate solution and stirred for 30 min at room temperature. The obtained solution was thermally treated at 160°C for 8 h in a

100 mL Teflon-lined stainless-steel autoclave. After filtering and thoroughly washing with deionized water and absolute ethanol, the Bi_2MoO_6 products were obtained by drying the material at 60 °C for 12 h. The product was labeled as BMO.

Synthesis of $\text{Bi@Bi}_2\text{MoO}_6$: Core-shell $\text{Bi@Bi}_2\text{MoO}_6$ materials were prepared using the same process as Bi_2MoO_6 photocatalysts, apart from the solvothermal reaction time. The reaction times were prolonged to 12 h, 16 h, 20 h, 24 h, 28 h and 32 h to obtain $\text{Bi@Bi}_2\text{MoO}_6$ photocatalysts, labeled as B@BMO-1, B@BMO-2, B@BMO-3, B@BMO-4, B@BMO-5 and B@BMO-6, respectively.

2.3. Characterization of Photocatalysts

The phase compositions of the samples were examined by powder XRD (Smart Lab 3 KW). A scanning electron microscope (SEM) (Sigma500, Carl Zeiss AG, Oberkochen, Germany) and transmission electron microscope (TEM) with an electron acceleration energy of 200 kV (JEM 2100F, JEOL, Tokyo, Japan) were employed to assess the morphology and structure. The chemical states and surface compositions of the samples were determined using an X-ray photoelectron spectrometer (ESCALAB Xi+, Thermo Fisher Scientific, Waltham, MA, USA), and the C 1s peak at 284.8 eV was used as a reference to calibrate the peak positions, and the peaks were fitted using Avantage. The UV-vis absorption spectra were acquired for the dry-pressed disk samples using a Scan UV-vis spectrophotometer, applying pure BaSO_4 as the reflectance sample. Time-resolved PL decay curves were obtained using a FLS980 fluorescence lifetime spectrophotometer (Edinburgh Instruments, Edinburgh, UK), and the decay curves were fitted to a triple-exponential model. Inductively coupled plasma mass spectrometry (ICP-MS) was used to determine the metal content.

2.4. Photoelectrochemical Measurements

Photoelectrochemical tests were performed on an electrochemical workstation (Model CHI 760D, CH instruments, Inc., Austin, TX, USA). The workstation was connected to a three-electrode system consisting of a working electrode, a counter electrode (Pt sheet) and a reference electrode (Ag/AgCl). To prepare the working electrode, 10 mg of photocatalysts, 10 μL of Trillatone X-100, 20 μL of acetylacetone and 80 μL of deionized water were ground and mixed well to coat the marked area (1 cm \times 1 cm) on a piece of 2 cm \times 1 cm FTO glass. The electrode was calcined at 200 °C for 2 h. The transient photocurrent responses were carried out in Na_2SO_4 aqueous solution under 300 W Xe lamp irradiation without any filters. Electrochemical impedance spectroscopy (EIS) was carried out in the frequency range of 0.005–10,000 Hz. The potential (vs. Ag/AgCl) was adjusted to (vs. NHE) by the equation as follows [37]:

$$E \text{ (vs. NHE)} = E \text{ (vs. Ag/AgCl)} + 0.197 \text{ V} + 0.0591 \times \text{pH} \quad (1)$$

2.5. Photocatalytic N_2 Fixation Reaction

The photocatalytic N_2 reduction reaction was carried out under mild conditions. A total of 10 mg of photocatalyst was dispersed in 25 mL of DI water ultrasonically for 10 min, and then the suspension liquid was transferred to a photocatalytic quartz reactor to catalyze the N_2 reduction reaction. The suspension was vigorously stirred in the dark for 30 min, and high-purity N_2 (100 mL min^{-1}) was bubbled to eliminate dissolved oxygen and saturate dissolved N_2 . The 300 W Xe lamp was used as a simulated light source. During the irradiation process, 3 mL of the solution was taken out every 30 min and filtered through a 0.22 μm MCE membrane to remove the photocatalyst. The concentration of ammonia (NH_4^+) was detected using the indophenol blue method at 655 nm on a UV-Vis spectrophotometer.

2.6. Determination of Ammonia

The amount of NH_3 in the reaction solution was determined using the indophenol blue method. Specifically, 2 mL of 1 M NaOH solution was added to the solution containing

salicylic acid and sodium citrate. After that, 1 mL of 0.05 M NaClO and 0.2 mL of the $C_3FeN_6Na_2O$ solution (1%wt) were sequentially added to 2 mL reaction solution. Placing at room temperature for 30 min, the NH_3 concentration was determined through the standard curve of NH_3 using a UV-Vis absorption spectrometer, measuring the absorbance at 655 nm.

3. Results and Discussion

3.1. The Structure of Samples

As a photoactive semiconductor, Bi_2MoO_6 nanosheets have been prepared for the construction of Schottky junction photocatalysts. In such a reaction system, ethylene glycol is a reducing agent. Through controlling the solvothermal reaction time, Bi^{3+} ions are in situ reduced to the metal Bi microsphere as a core, while Bi_2MoO_6 nanosheets are loaded onto the surface of the Bi microsphere as the shell (Figure 1a). The core-shell $Bi@Bi_2MoO_6$ composite in situ growth not only solves the problems that resulted from foreign elements but also benefits the formation of an intimate interface between Bi and Bi_2MoO_6 , which would accelerate the separation and transfer of photo-generated electrons and holes, thereby promoting photocatalytic activity. XRD patterns are used to examine the crystalline phase and composition of composites (Figure 1b). The diffraction peaks of pure Bi_2MoO_6 are perfectly indexed as orthorhombic Bi_2MoO_6 (PDF 84-0787). For the $Bi@Bi_2MoO_6$ composites, additional diffraction peaks which are derived from metal Bi (PDF 85-1329) are obviously discernable, suggesting the successful preparation of $Bi@Bi_2MoO_6$ composites. A possible growth mechanism has been proposed as similar as the previous report [42]. Firstly, the hydrolysis reaction of $[MoO_4]^{2-}$ into H_2MoO_4 occurs (Equation (2)). Then, it would react with Bi^{3+} in the solution to form Bi_2MoO_6 through an ion-exchange process (Equation (3)), which is the reason why only Bi_2MoO_6 is observed in the reaction time less than 12 h. By increasing the reaction time, the diffraction characteristic peaks associated with metal Bi (012), (104) and (110) can be clearly observed, and the diffraction peak intensity of metal Bi gradually increases, which indicates that Bi_2MoO_6 is in situ reduced to metal Bi by ethylene glycol (Equation (4)). The results of XRD confirm our predictions as well as the reaction process.

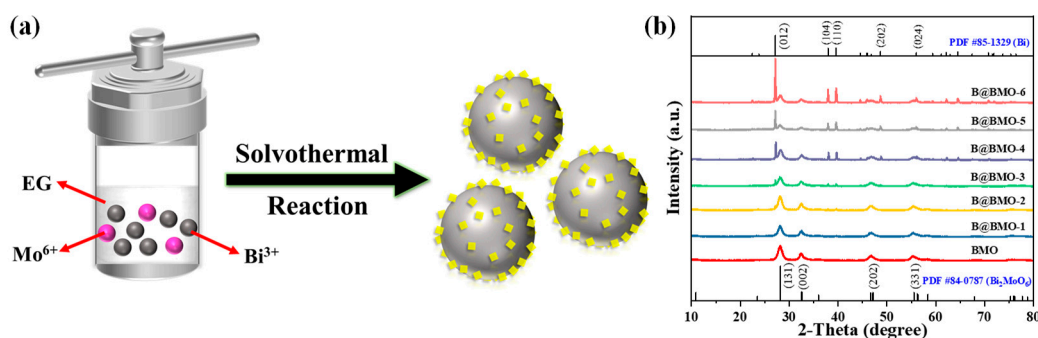
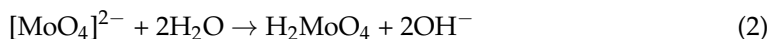


Figure 1. (a) Schematics of preparation of core-shell $Bi@Bi_2MoO_6$ composites; (b) XRD patterns of Bi_2MoO_6 materials and $Bi@Bi_2MoO_6$ composites.

The SEM is used to check the morphology of Bi_2MoO_6 materials and $Bi@Bi_2MoO_6$ composites. As shown in Figure 2a, Bi_2MoO_6 presents a typical microsphere-like structure with a diameter of 700 nm, which is formed by the accumulation of nanoparticles. For $B@BMO-1$, nanoparticles become nanosheets due to the Ostwald ripening process, while the morphology still keeps the microsphere structure (Figure 2b). At this stage, the crystal

is mainly composed of Bi_2MoO_6 , which agrees well with the results of XRD. Differently, B@BMO-2 exhibits a typical core-shell structure with a smooth sphere as the core and nanosheets as the shell (Figure 2c). According to the results, it can be concluded that the smooth sphere may be the metal Bi and the nanosheets may be the Bi_2MoO_6 due to the different morphology. Additionally, the longer the reaction time, the bigger the Bi spheres (Figure 2d–g). As shown in Figure 2h, a possible growth process of the $\text{Bi@Bi}_2\text{MoO}_6$ composite is considered, which is in agreement with the results of XRD and reaction equations. The related energy-dispersive X-ray (EDX) elemental mapping measurements are also investigated to determine the element distribution. The results are shown in Figure 2i–l, which indicate that Bi_2MoO_6 nanosheets are uniformly distributed on the surface of the Bi sphere, further demonstrating the formation of core-shell $\text{Bi@Bi}_2\text{MoO}_6$ composites.

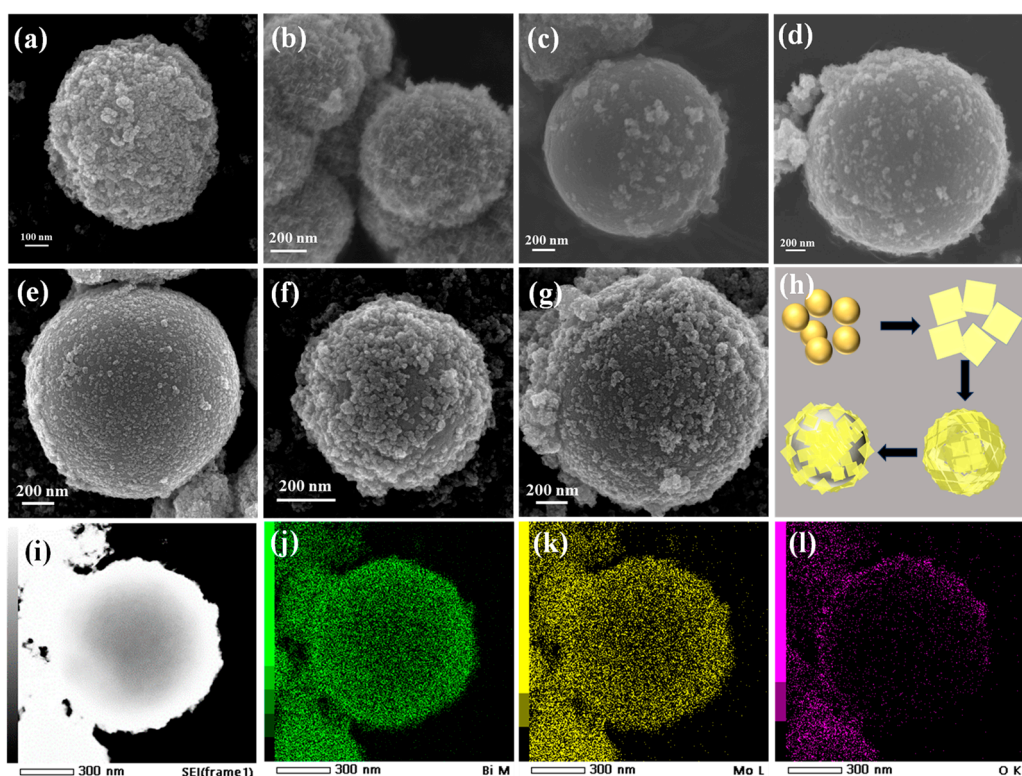


Figure 2. SEM images of BMO (a), B@BMO-1 (b), B@BMO-2 (c), B@BMO-3 (d), B@BMO-4 (e), B@BMO-5 (f) and B@BMO-6 (g), and the schematic diagram of the growth mechanism (h), and the elemental mapping images of Bi, Mo and O for the $\text{Bi@Bi}_2\text{MoO}_6$ composite (i–l).

To further determine the core-shell structure of $\text{Bi@Bi}_2\text{MoO}_6$ photocatalysts, the TEM and HRTEM images of Bi_2MoO_6 materials and $\text{Bi@Bi}_2\text{MoO}_6$ composites are shown in Figure 3. It can be found that pure Bi_2MoO_6 hierarchical structures are composed of ultrathin nanosheets with a thickness of ~ 20 nm and diameters in the range of $1\text{--}2$ μm , which are shown in Figure 3a,b. From the high-magnification TEM images of Bi_2MoO_6 (Figure 3c), the clear lattice fringes with a spacing of 0.314 nm can be seen, which corresponds to the (131) crystal faces of Bi_2MoO_6 in the orthogonal phase. Figure 3d shows the TEM images of the B@BMO-4 sample. It can be observed that the very black smooth sphere with a diameter of about 1 μm is the core, and numerous ultrathin nanosheets with a transparent structure are stacked on the surface of the black sphere as the shell, which agrees with the results of the SEM. The results further confirm the successful formation of core-shell $\text{Bi@Bi}_2\text{MoO}_6$ composites. Moreover, the HRTEM images of the region with a green rectangle for the B@BMO-4 composite indicated the well-matched (131) plane of Bi_2MoO_6 with a lattice spacing of 0.315 and 0.314 nm (Figure 3e,f). The red rectangle for the B@BMO-4 composite corresponds to the (012) lattice plane of metal Bi particles with a lattice spacing of 0.328 nm,

which is consistent with the XRD results. The TEM images of the B@BMO-6 sample are shown in Figure 3g,i; it can be found that the morphology of the B@BMO-6 sample is similar to that of B@BMO-4 with the core-shell structure which would have the benefit of photo-generated carrier separation and transfer.

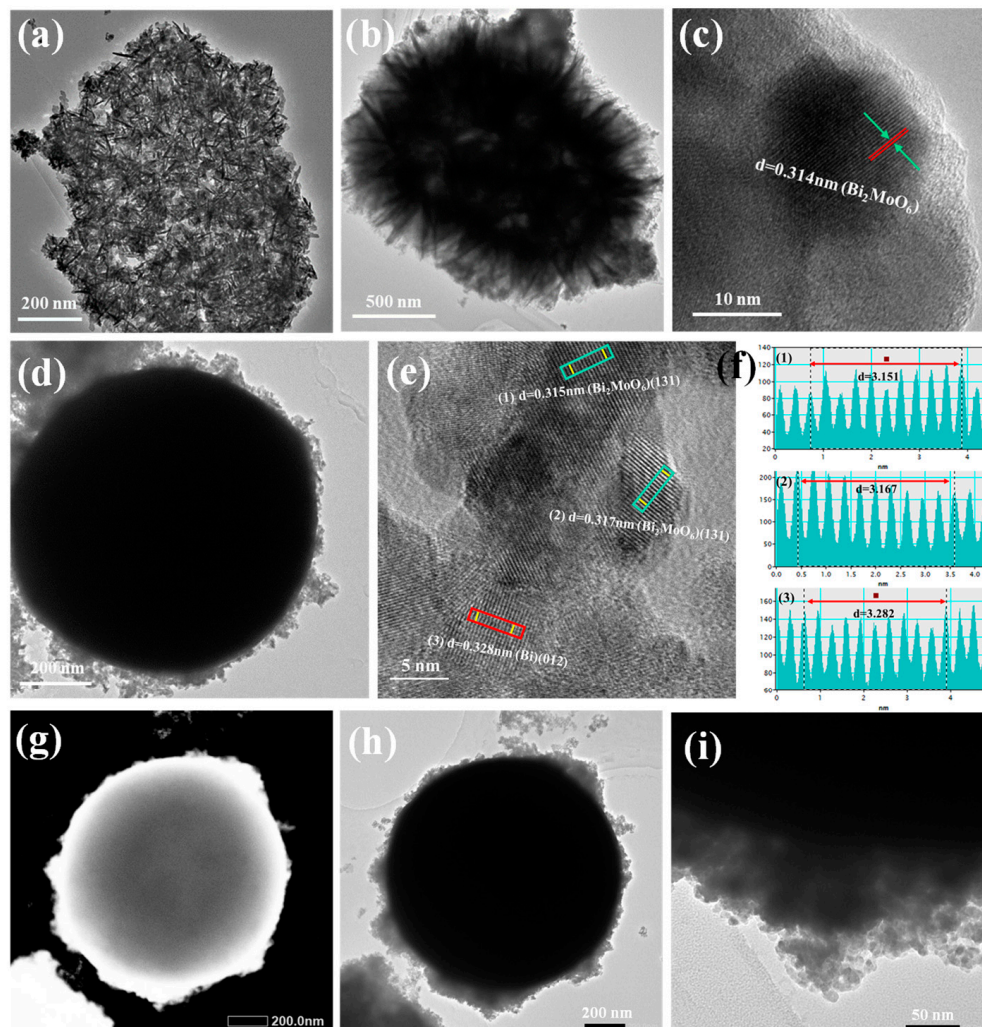


Figure 3. TEM and HRTEM images of BMO (a–c), B@BMO-4 (d–f) and B@BMO-6 (g–i).

To further understand the chemical compositions of BMO, B@BMO-4 and B@BMO-6, an X-ray photoelectron spectroscopy (XPS) measurement is carried out. As shown in Figure 4a, the surveys of three samples indicate that all the samples consist of Bi, Mo and O elements. All binding energy is calibrated with the C 1s band at 284.8 eV. The high-resolution XPS spectra of Bi 4f are displayed in Figure 4b. The binding energies located at 159.24 and 164.53 eV are attributed to Bi 4f_{7/2} and Bi 4f_{5/2}, respectively, and no other bands can be observed, which demonstrated the existence of only Bi³⁺ for BMO samples [43]. Apart from the binding energies located at 159.11 and 164.42 eV that correspond to Bi 4f_{7/2} and Bi 4f_{5/2} of Bi³⁺, there are new two bands at 156.56 and 161.93 eV which are attributed to the metal Bi for B@BMO-4, suggesting the in situ formation of surface-detectable Bi due to the reduction reaction with the increase in reaction time. It can be seen that the intensity of bands at 156.49 and 161.85 eV increases for B@BMO-6, indicating more metal Bi is reduced. The Mo bands are divided into two bands at 232.45 and 235.60 eV assigned to Mo 3d_{5/2} and Mo 3d_{3/2}, which are assigned to the bands of Mo⁶⁺ in Bi₂MoO₆ [44]. For B@BMO samples, there is a negative shift of about 0.1 eV in Mo 3d spectra as compared to that of BMO. In addition, the two bands of BMO at 231.43 and 234.51 eV are typical of Mo⁵⁺ cations,

which indicates the introduction of some oxygen vacancies during metal Bi reduction [33]. Moreover, an obviously negative shift in Bi XPS spectra is also observed which suggests a strong interaction between metal Bi and Bi_2MoO_6 [45]. For the O 1s spectra (Figure 4d), two bands located at 530.01 and 530.81 eV correspond to the lattice and defect oxygen of Bi_2MoO_6 , respectively [46].

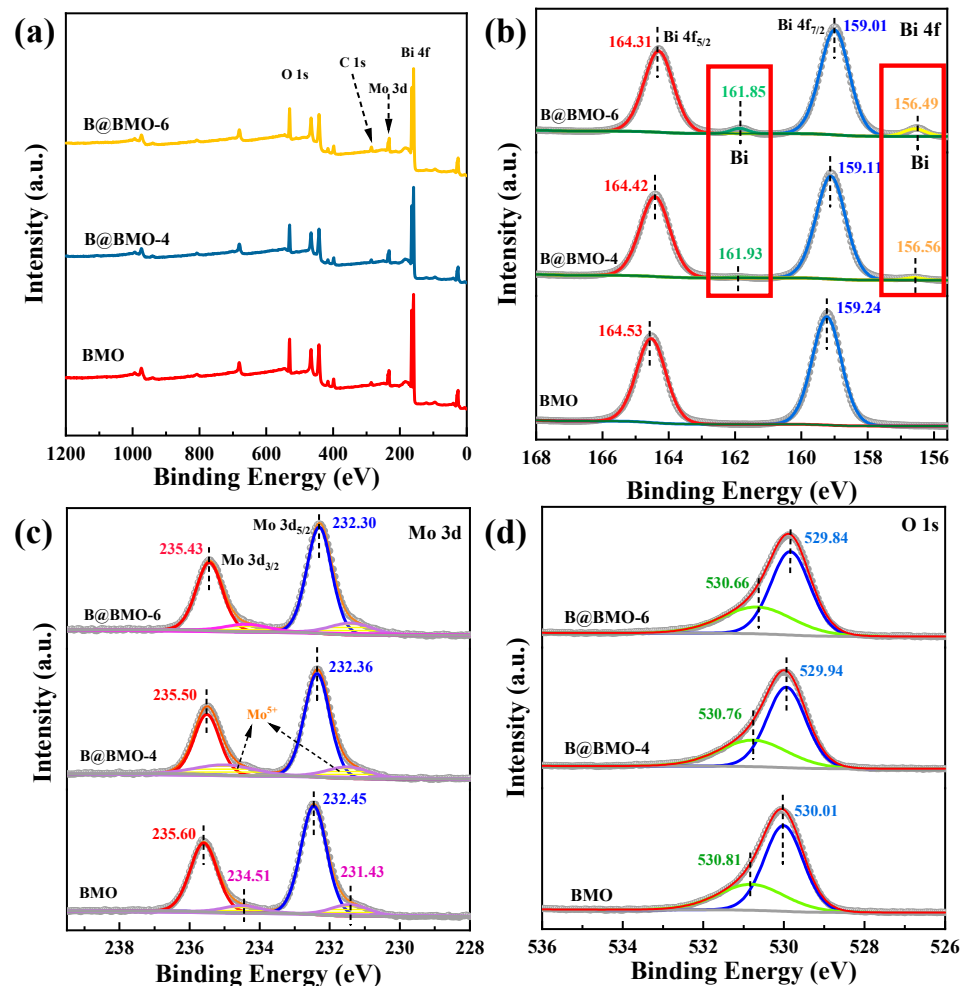


Figure 4. XPS spectra of BMO, B@BMO-4 and B@BMO-6 of survey (a), Bi 4f (b), Mo 3d (c) and O 1s (d).

3.2. Photoelectrochemical Properties and Photocatalytic N_2 to NH_3

UV–vis DRS measurement is performed to study the light harvesting capability of the as-synthesized photocatalysts. As displayed in Figure 5a, B@BMO photocatalysts have strong visible light absorption compared with Bi_2MoO_6 due to the localized surface plasma resonance (LSPR) of metal Bi [47,48]. Pristine Bi_2MoO_6 has light absorption at 485 nm corresponding to the band gap of 2.56 eV, as shown in Figure 5b [32]. The introduction of metal Bi greatly improves the absorption efficiency for Bi_2MoO_6 , and the colors of B@BMO photocatalysts gradually change from light yellow to dark gray (inset of Figure 5a), also suggesting the improvement in visible light absorption. The Mott–Schottky measurement is usually used to determine the conduction band minimum (CBM) position. The CBM potential of Bi_2MoO_6 is calculated to be -0.52 V vs. NHE which is about 0–0.2 eV more negative than the flat-band potential and that of $\text{Bi@Bi}_2\text{MoO}_6$ -4 is -0.63 V vs. NHE (Figure 5c). To reveal the charge separation efficiency, a time-resolved technique has been carried out. The electron lifetimes of the fitting results for Bi_2MoO_6 are 1.078 ns for τ_1 , 6.897 ns for τ_2 and 1.08 ns for average τ , respectively (Figure 5d). In comparison to Bi_2MoO_6 , B@BMO photocatalysts have a longer PL lifetime. For the B@BMO-4 composite, τ_1 is 1.623 ns, τ_2 is 1.355 ns and average τ is 1.62 ns, respectively. The long lifetime demonstrates that the

Schottky junction by the introduction of metal Bi on Bi_2MoO_6 could effectively spur the charge separation and elongate the carrier lifetime. The measurements of photoelectrochemistry are also performed to further study the charge separation at the interface between Bi and Bi_2MoO_6 . The transient photocurrent responses of BMO and B@BMO composites are presented in Figure 5e. The current densities of all of the samples are near zero in the dark as the reference. Once the light is turned on, a very large pulse can be observed which indicates more electrons produced. The photocurrent generated by pristine Bi_2MoO_6 is very low (inset of Figure 5e), while the B@BMO composites exhibit enhanced photocurrent density. Also, B@BMO-4 has the highest photocurrent among the B@BMO composites, which demonstrates that more photo-generated electrons are produced in the Schottky junction under irradiation, thereby promoting the efficient separation of core-shell B@BMO photocatalysts. The EIS is shown in Figure 5f by displaying it as Nyquist plots, which can obtain the resistance of the charges through the fitting. The diameter is small which indicates the resistance is small, which indicates an efficient charge transfer from the electrode to the solution due to the Schottky junction. The diameters of B@BMO composites are smaller than that of BMO. The impedance data are obtained through fitting the equivalent circuit. The R_1 , R_2 and CPE1 represent the resistance of electrode, the resistance of transfer and the double-layer capacitance element, respectively. B@BMO-4 has the lowest R_2 of about $45,032 \Omega$ among all B@BMO photocatalysts. The results of the electrochemical measurements indicate that the core-shell Schottky junction not only promotes the separation of electrons on the semiconductor but also accelerates the interfacial transfer from Bi_2MoO_6 to metal Bi, just like as reported by previous articles [22].

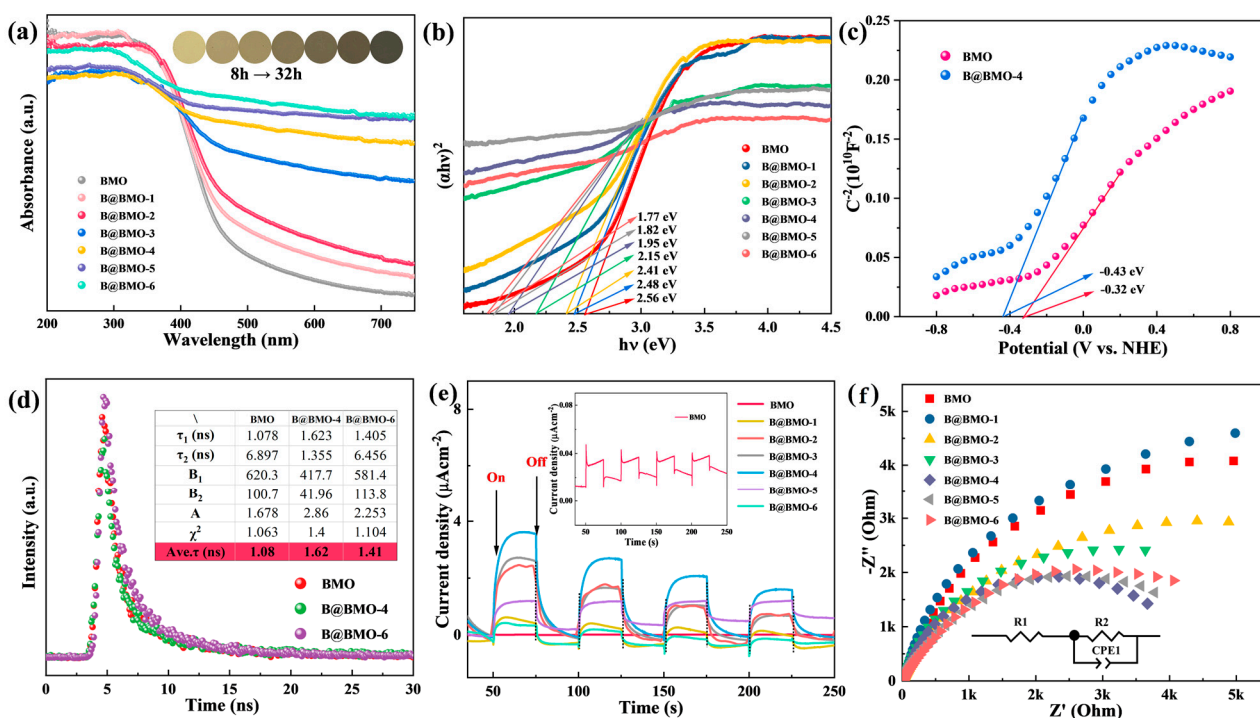


Figure 5. (a) UV-vis diffuse reflectance spectra (DRS), (b) band gaps of all samples, (c) Mott–Schottky curves of BMO and B@BMO-4, (d) time-resolution PL spectra, (e) transient photocurrent response under 300 W Xe lamp, (f) electrochemical impedance spectroscopy (EIS).

The photoactivities of core-shell $\text{Bi@Bi}_2\text{MoO}_6$ composites for N_2 -to-ammonia conversion have been investigated using deionized water without any scavenger. The produced NH_3 is spectrophotometrically measured based on the indophenol blue method [49]. The amount of ammonia over Bi_2MoO_6 and core-shell $\text{Bi@Bi}_2\text{MoO}_6$ composites with different contents of metal Bi confirmed by the ICP measurement is shown in Figure 6a. The rate of photocatalytic nitrogen to ammonia on pure Bi_2MoO_6 is $35.70 \mu\text{mol g}^{-1} \text{h}^{-1}$, but the

generation rate of ammonia increases to $42.74 \mu\text{mol g}^{-1} \text{h}^{-1}$ when metal Bi is self-reduced onto Bi_2MoO_6 to $\text{Bi@Bi}_2\text{MoO}_6$ core-shell composites (B@BMO-2) due to the increase in Bi active sites. With the increase in the Bi amount, the efficiency of the N_2 -to-ammonia conversion also increases and achieves a maximum ($86.00 \mu\text{mol g}^{-1} \text{h}^{-1}$) when the content of Bi is about 0.17% (B@BMO-4 photocatalyst). While the amount of Bi increases further, the yield of the photocatalytic N_2 -to-ammonia conversion decreases. The result indicates that the activity of the photocatalytic nitrogen-to-ammonia conversion on $\text{Bi@Bi}_2\text{MoO}_6$ core-shell composites is not a linearly dependent relationship. There is an optimal value of metal Bi. When more Bi precursors are self-reduced to metal Bi, the amount of Bi_2MoO_6 would decrease which results in the decrease of light absorption, thus further influencing the photocatalytic N_2 -to-ammonia conversion. However, when more Bi precursors generate a Bi_2MoO_6 semiconductor, the amount of Bi is very small which results in the decrease in catalytic reaction due to the lack of more Bi active sites. As a result, the activity of the photocatalytic nitrogen-to-ammonia conversion on $\text{Bi@Bi}_2\text{MoO}_6$ core-shell composites would present a volcano-type curve. The dependence on the reaction time over the most excellent $\text{Bi@Bi}_2\text{MoO}_6$ composite (B@BMO-4) is also explored. The photocatalytic activity for ammonia conversion presents a remarkably linear enhancement (Figure 6b). Under irradiation, the B@BMO-4 photocatalyst could produce NH_3 with a value of $173.40 \mu\text{mol g}^{-1}$ for 2 h. A comparison in NH_3 production between $\text{Bi@Bi}_2\text{MoO}_6$ nanospheres and some typical photocatalysts in previous reports has been summarized in Table S1. In order to confirm the source of nitrogen, the blank experiment without any photocatalyst under irradiation has also been carried out, and the result is shown in Figure 6c. It can be seen that there is a trace amount of ammonia detected as the background, which is subtracted when quantifying ammonia production. Furthermore, the other controlled experiments over $\text{Bi@Bi}_2\text{MoO}_6$ composites under different conditions are shown in Figure 6d. Under the condition without the photocatalyst, there is no ammonia detected under N_2 and irradiation. Such a scenario is also observed under the conditions of air and Ar atmospheres. However, an obvious enhancement in the photocatalytic N_2 reduction reaction can be seen in the $\text{Bi@Bi}_2\text{MoO}_6$ composite under the N_2 atmosphere, which indicates that the N element is derived from incoming N_2 . To further demonstrate the stability of the photocatalyst, a longer cycle test is performed (Figure 6e). The results show that the $\text{Bi@Bi}_2\text{MoO}_6$ composite still has strong photocatalytic nitrogen fixation activity after five cycles (30 min each reaction time). In addition, the crystallinity and morphology of the photocatalyst before and after the reaction are measured (Figure 6f). The results show that the $\text{Bi@Bi}_2\text{MoO}_6$ composite has good stability, indicating that the formation of a core-shell $\text{Bi@Bi}_2\text{MoO}_6$ composite is beneficial in improving the photocatalytic performance of N_2 to NH_3 .

3.3. Mechanism

The absorption wavelength of Bi_2MoO_6 is approximately 480 nm and that of $\text{Bi@Bi}_2\text{MoO}_6$ -4 is about 635 nm. In addition, the optical band gaps are calculated, and the Mott-Schottky measurements of Bi_2MoO_6 and $\text{Bi@Bi}_2\text{MoO}_6$ -4 have been performed. From the results, it can be found that the band gap energy of Bi_2MoO_6 is calculated from the absorption spectrum to be 2.56 eV, which is consistent with previous reports [42]. The band gap value of $\text{Bi@Bi}_2\text{MoO}_6$ -4 is about 1.95 eV, which is narrower than that of Bi_2MoO_6 owing to the localized surface plasmon resonance of metal Bi. The valence band maximum (VBM) potential of Bi_2MoO_6 is about 2.04 V vs. NHE using the equation, $\text{VBM} = \text{CBM} - E_g$. Similarly, the VBM potential of $\text{Bi@Bi}_2\text{MoO}_6$ -4 is about 1.32 V vs. NHE. According to the results of UV-vis DRS and Mott-Schottky measurements, the schematic diagrams of the energy band arrangement of Bi_2MoO_6 and $\text{Bi@Bi}_2\text{MoO}_6$ -4 have been shown in Figure 7a.

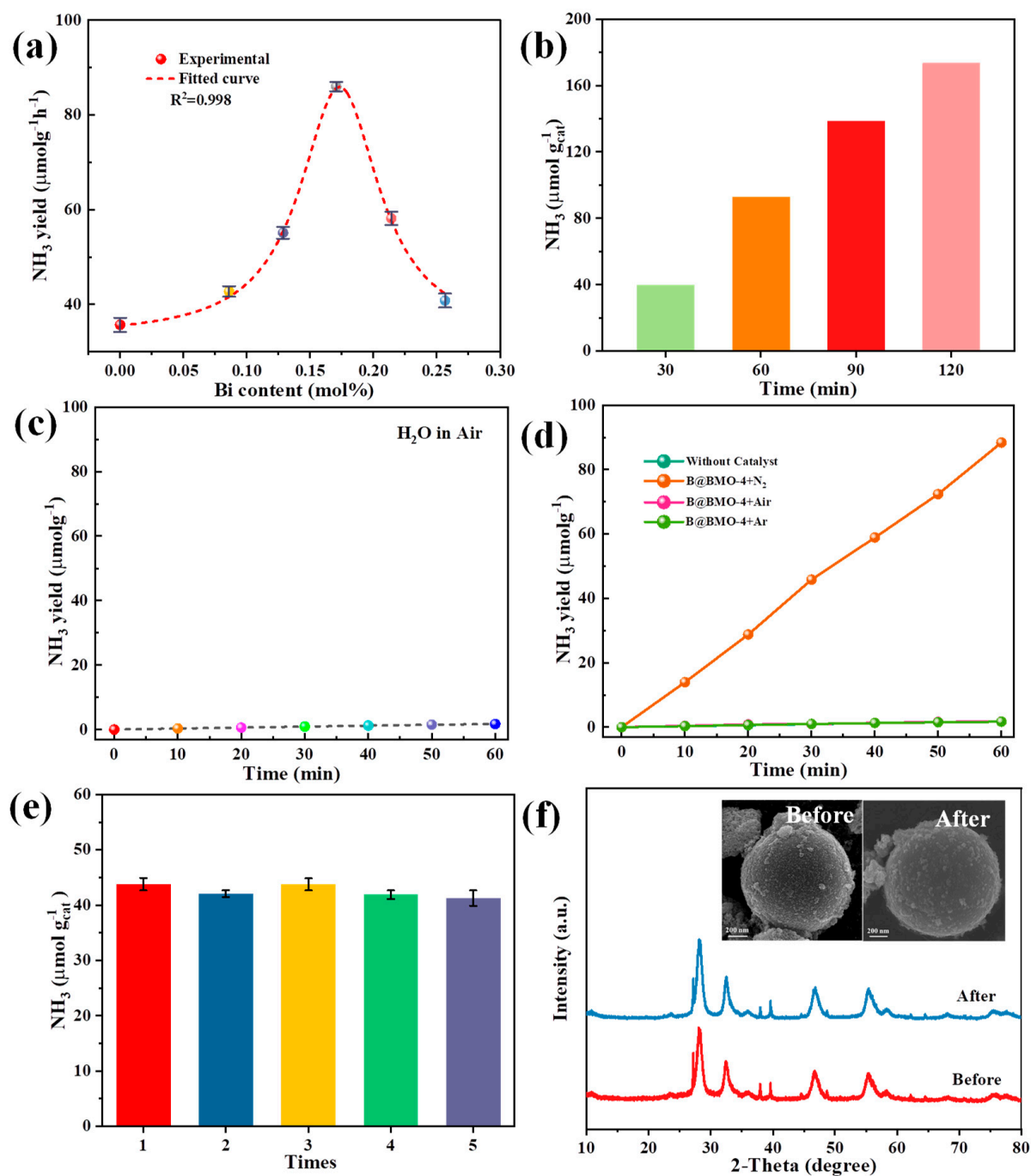


Figure 6. (a) Dependence of photocatalytic ammonia production on metallic Bi in Bi@Bi₂MoO₆ composites under 300 W Xe lamp irradiation, (b) dependence of photocatalytic ammonia production on reaction time, (c) blank experiment without photocatalyst, (d) controlled experiments for photocatalytic ammonia production over Bi@Bi₂MoO₆ composites under different conditions, (e) photostability of Bi@Bi₂MoO₆ photocatalysts for ammonia production and (f) XRD patterns and SEM images of B@BMO-4 before and after photocatalytic ammonia production.

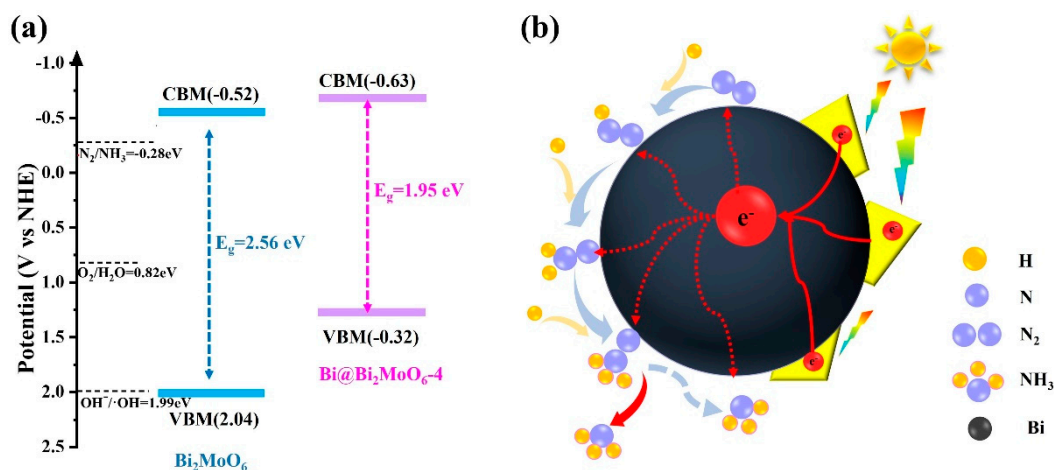


Figure 7. (a) The band structure of Bi_2MoO_6 and $\text{Bi@Bi}_2\text{MoO}_6\text{-4}$; (b) schematics of the photocatalytic N_2 -to-ammonia conversion over core-shell $\text{Bi@Bi}_2\text{MoO}_6$ photocatalysts.

Currently, there are two different associative N_2 hydrogenation pathways, including the distal pathway and alternating pathway which are usually considered [50,51]. Some theoretical investigations reported that N_2 favored adsorbing at Bi sites with unsaturated coordination through an end-on bound structure [35]. According to the above results and some investigations, a possible distal pathway mechanism of the photocatalytic N_2 -to-ammonia conversion over the core-shell $\text{Bi@Bi}_2\text{MoO}_6$ composite has been proposed (Figure 7b). In this distal pathway, N_2 adsorbs on metallic Bi with the end-on bound structure. One of the N atoms on the surface is hydrogenated successively until NH_3 is formed and released. On the basis of this pathway, only NH_3 is produced. Actually, other nitrogen species have not been detected during photocatalytic N_2 fixation over $\text{Bi@Bi}_2\text{MoO}_6$ photocatalysts, which further confirms the distal pathway.

4. Conclusions

In this work, a core-shell $\text{Bi@Bi}_2\text{MoO}_6$ photocatalyst through constructing Schottky junctions is explored for N_2 reduction to ammonia. Metal Bi not only promotes the photo-generated electron and hole separation owing to the Schottky junction at the interface of Bi and Bi_2MoO_6 but also improves N_2 adsorption and activation at Bi active sites through an end-on bound structure synchronously. As a result, the yield of the photocatalytic N_2 -to-ammonia conversion reaches up to $173.40 \mu\text{mol g}^{-1}$ on core-shell $\text{Bi@Bi}_2\text{MoO}_6$ photocatalysts, as much as two times of that of bare Bi_2MoO_6 . This work provides a new design for the decarbonization of the nitrogen reduction reaction by the utilization of renewable energy sources.

Supplementary Materials: The following supporting information can be downloaded at: <https://www.mdpi.com/article/10.3390/nano14090780/s1>, Table S1. Comparison of photocatalytic N_2 reduction activity on Bi-based photocatalysts. References [22,24,36,43,52–65] are cited in the Supplementary Materials.

Author Contributions: Formal analysis, G.W.; Investigation, M.W. and R.L.; Data curation, M.W. and M.Y.; Supervision, G.L. and Y.P. All authors have read and agreed to the published version of the manuscript.

Funding: The work was supported by the National Natural Science Foundation of China (22005164), the Natural Foundation of Shandong Province (No. BS2015CL002), and Basic Research Project of Qingdao Source Innovation Program Fund (17-1-1-82-jch).

Data Availability Statement: Data are contained within the article.

Conflicts of Interest: The authors declare no conflict of interest.

References

1. Huang, Z.; Yang, B.; Zhou, Y.; Luo, W.; Chen, G.; Liu, M.; Liu, X.; Ma, R.; Zhang, N. Tungsten Nitride/Tungsten Oxide Nanosheets for Enhanced Oxynitride Intermediate Adsorption and Hydrogenation in Nitrate Electroreduction to Ammonia. *ACS Nano* **2023**, *17*, 25091–25100. [[CrossRef](#)] [[PubMed](#)]
2. Fu, X.; Pedersen, J.B.; Zhou, Y.; Saccoccio, M.; Li, S.; Salinas, R.; Li, K.; Andersen, S.Z.; Xu, A.; Deissler, N.H.; et al. Continuous-flow electrosynthesis of ammonia by nitrogen reduction and hydrogen oxidation. *Science* **2023**, *379*, 707–712. [[CrossRef](#)] [[PubMed](#)]
3. Zhou, N.; Wang, Z.; Zhang, N.; Bao, D.; Zhong, H.; Zhang, X. Potential-Induced Synthesis and Structural Identification of Oxide-Derived Cu Electrocatalysts for Selective Nitrate Reduction to Ammonia. *ACS Catal.* **2023**, *13*, 7529–7537. [[CrossRef](#)]
4. Kisch, H. In the Light and in the Dark: Photocatalytic Fixation of Nitrogen into Ammonia and Nitrate at Iron Titanate Semiconductor Thin Films. *Eur. J. Inorg. Chem.* **2020**, *2020*, 1376–1382. [[CrossRef](#)]
5. Wang, T.; Abild-Pedersen, F. Achieving industrial ammonia synthesis rates at near-ambient conditions through modified scaling relations on a confined dual site. *Proc. Natl. Acad. Sci. USA* **2021**, *118*, e2106527118. [[CrossRef](#)] [[PubMed](#)]
6. Reichle, S.; Felderhoff, M.; Schuth, F. Mechanocatalytic Room-Temperature Synthesis of Ammonia from Its Elements Down to Atmospheric Pressure. *Angew. Chem. Int. Ed.* **2021**, *60*, 26385–26389. [[CrossRef](#)]
7. Liu, S.; Wang, M.; Ji, H.; Zhang, L.; Ni, J.; Li, N.; Qian, T.; Yan, C.; Lu, J. Solvent-in-Gas System for Promoted Photocatalytic Ammonia Synthesis on Porous Framework Materials. *Adv. Mater.* **2023**, *35*, 202211730. [[CrossRef](#)]
8. Ren, G.; Zhao, J.; Zhao, Z.; Li, Z.; Wang, L.; Zhang, Z.; Li, C.; Meng, X. Defects-Induced Single-Atom Anchoring on Metal-Organic Frameworks for High-Efficiency Photocatalytic Nitrogen Reduction. *Angew. Chem. Int. Ed.* **2024**, *63*, 202314408. [[CrossRef](#)]
9. Wu, R.; Gao, S.; Jones, C.; Sun, M.; Guo, M.; Tai, R.; Chen, S.; Wang, Q. Bi/BSO Heterojunctions via Vacancy Engineering for Efficient Photocatalytic Nitrogen Fixation. *Adv. Funct. Mater.* **2024**, 2314051. [[CrossRef](#)]
10. Linnik, O.; Kisch, H. On the mechanism of nitrogen photofixation at nanostructured iron titanate films. *Photochem. Photobiol. Sci.* **2006**, *5*, 938–942. [[CrossRef](#)]
11. Yang, H.; Ren, G.; Li, Z.; Zhang, Z.; Meng, X. Fast Joule heating for transformation of Fe-MIL-125(Ti) to Fe/TiO₂ with enhanced photocatalytic activity in N₂ fixation. *Appl. Catal. B-Environ. Energy* **2024**, *347*, 123795. [[CrossRef](#)]
12. Gao, W.; Li, X.; Luo, S.; Luo, Z.; Zhang, X.; Huang, R.; Luo, M. In situ modification of cobalt on MXene/TiO₂ as composite photocatalyst for efficient nitrogen fixation. *J. Colloid Interface Sci.* **2021**, *585*, 20–29. [[CrossRef](#)]
13. Li, X.; Yang, L.; Liu, Q.; Bai, W.; Li, H.; Wang, M.; Qian, Q.; Yang, Q.; Xiao, C.; Xie, Y. Directional Shunting of Photogenerated Carriers in POM@MOF for Promoting Nitrogen Adsorption and Oxidation. *Adv. Mater.* **2023**, *35*, 202304532. [[CrossRef](#)]
14. Yang, J.; Bai, H.; Guo, Y.; Zhang, H.; Jiang, R.; Yang, B.; Wang, J.; Yu, J.C. Photodriven Disproportionation of Nitrogen and Its Change to Reductive Nitrogen Photofixation. *Angew. Chem. Int. Ed.* **2020**, *60*, 927–936. [[CrossRef](#)] [[PubMed](#)]
15. Kumar, A.; Sharma, M.; Sheoran, S.; Jaiswal, S.; Patra, A.; Bhattacharya, S.; Krishnan, V. Tailoring defects in SrTiO₃ by one step nanoarchitectonics for realizing photocatalytic nitrogen fixation in pure water. *Nanoscale* **2023**, *15*, 11667–11680. [[CrossRef](#)]
16. Pournemati, K.; Habibi-Yangjeh, A.; Khataee, A. TiO₂ Quantum Dots/Fe₃S₄ Heterojunction Nanocomposites for Efficient Ammonia Production through Nitrogen Fixation upon Simulated Sunlight. *ACS Appl. Nano Mater.* **2024**, *7*, 2200–2213. [[CrossRef](#)]
17. Vu, V.T.; Vu, T.T.H.; Phan, T.L.; Kang, W.T.; Kim, Y.R.; Tran, M.D.; Nguyen, H.T.T.; Lee, Y.H.; Yu, W.J. One-Step Synthesis of NbSe₂/Nb-Doped-WSe₂ Metal/Doped-Semiconductor van der Waals Heterostructures for Doping Controlled Ohmic Contact. *ACS Nano* **2021**, *15*, 13031–13040. [[CrossRef](#)] [[PubMed](#)]
18. Yang, J.; Li, L.; Xiao, C.; Xie, Y. Dual-Plasmon Resonance Coupling Promoting Directional Photosynthesis of Nitrate from Air. *Angew. Chem. Int. Ed.* **2023**, *62*, 202311911. [[CrossRef](#)]
19. Liu, Y.; Cheng, M.; He, Z.; Gu, B.; Xiao, C.; Zhou, T.; Guo, Z.; Liu, J.; He, H.; Ye, B.; et al. Pothole-rich Ultrathin WO₃ Nanosheets that Trigger N≡N Bond Activation of Nitrogen for Direct Nitrate Photosynthesis. *Angew. Chem. Int. Ed.* **2019**, *58*, 731–735. [[CrossRef](#)]
20. Ren, W.; Mei, Z.; Zheng, S.; Li, S.; Zhu, Y.; Zheng, J.; Lin, Y.; Chen, H.; Gu, M.; Pan, F. Wavelength-Dependent Solar N₂ Fixation into Ammonia and Nitrate in Pure Water. *Research* **2020**, *2020*, 3750314. [[CrossRef](#)]
21. Xia, P.; Pan, X.; Jiang, S.; Yu, J.; He, B.; Ismail, P.M.; Bai, W.; Yang, J.; Yang, L.; Zhang, H.; et al. Designing a Redox Heterojunction for Photocatalytic “Overall Nitrogen Fixation” under Mild Conditions. *Adv. Mater.* **2022**, *34*, 202200563. [[CrossRef](#)] [[PubMed](#)]
22. Huang, Y.; Zhu, Y.; Chen, S.; Xie, X.; Wu, Z.; Zhang, N. Schottky Junctions with Bi Cocatalyst for Taming Aqueous Phase N₂ Reduction toward Enhanced Solar Ammonia Production. *Adv. Sci.* **2021**, *8*, 202003626. [[CrossRef](#)] [[PubMed](#)]
23. Zhang, H.; Zhang, P.; Zhao, J.; Liu, Y.; Huang, Y.; Huang, H.; Yang, C.; Zhao, Y.; Wu, K.; Fu, X.; et al. The Hole-Tunneling Heterojunction of Hematite-Based Photoanodes Accelerates Photosynthetic Reaction. *Angew. Chem. Int. Ed.* **2021**, *60*, 16009–16018. [[CrossRef](#)] [[PubMed](#)]
24. Wang, G.; Huo, T.; Deng, Q.; Yu, F.; Xia, Y.; Li, H.; Hou, W. Surface-layer bromine doping enhanced generation of surface oxygen vacancies in bismuth molybdate for efficient photocatalytic nitrogen fixation. *Appl. Catal. B Environ.* **2022**, *310*, 121319. [[CrossRef](#)]
25. Xue, X.; Chen, R.; Yan, C.; Hu, Y.; Zhang, W.; Yang, S.; Ma, L.; Zhu, G.; Jin, Z. Efficient photocatalytic nitrogen fixation under ambient conditions enabled by the heterojunctions of n-type Bi₂MoO₆ and oxygen-vacancy-rich p-type BiOBr. *Nanoscale* **2019**, *11*, 10439–10445. [[CrossRef](#)] [[PubMed](#)]
26. Wu, J.M.; Chen, Y.N. The surface plasmon resonance effect on the enhancement of photodegradation activity by Au/ZnSn(OH)₆ nanocubes. *Dalton Trans.* **2015**, *44*, 16294–16303. [[CrossRef](#)] [[PubMed](#)]

27. Wang, D.; Shen, H.; Guo, L.; Wang, C.; Fu, F.; Liang, Y. Ag/Bi₂MoO_{6-x} with enhanced visible-light-responsive photocatalytic activities via the synergistic effect of surface oxygen vacancies and surface plasmon. *Appl. Surf. Sci.* **2018**, *436*, 536–547. [[CrossRef](#)]
28. Dong, X.; Xu, L.; Ma, J.; Li, Y.; Yin, Z.; Chen, D.; Wang, Q.; Han, J.; Qiu, J.; Yang, Z.; et al. Enhanced interfacial charge transfer and photothermal effect via in-situ construction of atom co-sharing Bi plasmonic/Bi₄O₅Br₂ nanosheet heterojunction towards improved full-spectrum photocatalysis. *Chem. Eng. J.* **2023**, *459*, 141557. [[CrossRef](#)]
29. Fang, M.; Tan, X.; Liu, Z.; Hu, B.; Wang, X. Recent Progress on Metal-Enhanced Photocatalysis: A Review on the Mechanism. *Research* **2021**, *2021*, 9794329. [[CrossRef](#)]
30. He, W.; Xiong, J.; Tang, Z.; Wang, Y.; Wang, X.; Xu, H.; Zhao, Z.; Liu, J.; Wei, Y. Localized surface plasmon resonance effect of bismuth nanoparticles in Bi/TiO₂ catalysts for boosting visible light-driven CO₂ reduction to CH₄. *Appl. Catal. B-Environ. Energy* **2024**, *344*, 123651. [[CrossRef](#)]
31. Zhao, D.; Xuan, Y.; Zhang, K.; Liu, X. Highly Selective Production of Ethanol over Hierarchical Bi@Bi₂MoO₆ Composite via Bicarbonate-Assisted Photocatalytic CO₂ Reduction. *Chemsuschem* **2021**, *14*, 3293–3302. [[CrossRef](#)] [[PubMed](#)]
32. Zhao, Z.; Zhang, W.; Sun, Y.; Yu, J.; Zhang, Y.; Wang, H.; Dong, F.; Wu, Z. Bi Cocatalyst/Bi₂MoO₆ Microspheres Nanohybrid with SPR-Promoted Visible-Light Photocatalysis. *J. Phys. Chem. C* **2016**, *120*, 11889–11898. [[CrossRef](#)]
33. Xu, F.; Wang, J.; Zhang, N.; Liang, H.; Sun, H. Simultaneously generating Bi quantum dot and oxygen vacancy on Bi₂MoO₆ nanosheets for boosting photocatalytic selective alcohol oxidation. *Appl. Surf. Sci.* **2022**, *575*, 151738. [[CrossRef](#)]
34. Greeley, J.; Jaramillo, T.F.; Bonde, J.; Chorkendorff, I.B.; Norskov, J.K. Computational high-throughput screening of electrocatalytic materials for hydrogen evolution. *Nat. Mater.* **2006**, *5*, 909–913. [[CrossRef](#)] [[PubMed](#)]
35. Li, H.; Shang, J.; Ai, Z.; Zhang, L. Efficient Visible Light Nitrogen Fixation with BiOBr Nanosheets of Oxygen Vacancies on the Exposed {001} Facets. *J. Am. Chem. Soc.* **2015**, *137*, 6393–6399. [[CrossRef](#)] [[PubMed](#)]
36. Kok, S.H.W.; Lee, J.; Chong, W.K.; Ng, B.-J.; Kong, X.Y.; Ong, W.J.; Chai, S.-P.; Tan, L.-L. Bismuth-rich Bi₁₂O₁₇Cl₂ nanorods engineered with oxygen vacancy defects for enhanced photocatalytic nitrogen fixation. *J. Alloys Compd.* **2023**, *952*, 170015. [[CrossRef](#)]
37. Lan, M.; Zheng, N.; Dong, X.; Ma, H.; Zhang, X. One-step in-situ synthesis of Bi-decorated BiOBr microspheres with abundant oxygen vacancies for enhanced photocatalytic nitrogen fixation properties. *Colloids Surf. A-Physicochem. Eng. Asp.* **2021**, *623*, 126744. [[CrossRef](#)]
38. Li, X.; Zhao, C.; Wang, J.; Zhang, J.; Wu, Y.; He, Y. Cu-doped Bi/B₂WO₆ catalysts for efficient N₂ fixation by photocatalysis. *Front. Chem. Sci. Eng.* **2023**, *17*, 1412–1422. [[CrossRef](#)]
39. Geng, M.; Peng, Y.; Zhang, Y.; Guo, X.; Yu, F.; Yang, X.; Xie, G.; Dong, W.; Liu, C.; Li, J.; et al. Hierarchical ZnIn₂S₄: A promising cocatalyst to boost visible-light-driven photocatalytic hydrogen evolution of In(OH)₃. *Int. J. Hydrogen Energy* **2019**, *44*, 5787–5798. [[CrossRef](#)]
40. Guo, X.; Peng, Y.; Liu, G.; Xie, G.; Guo, Y.; Zhang, Y.; Yu, J. An Efficient ZnIn₂S₄@CuInS₂ Core-Shell p-n Heterojunction to Boost Visible-Light Photocatalytic Hydrogen Evolution. *J. Phys. Chem. C* **2020**, *124*, 5934–5943. [[CrossRef](#)]
41. Ren, X.; Liu, F.; Wu, H.; Lu, Q.; Zhao, J.; Liu, Y.; Zhang, J.; Mao, J.; Wang, J.; Han, X.; et al. Reconstructed Bismuth Oxide through in situ Carbonation by Carbonate-containing Electrolyte for Highly Active Electrocatalytic CO₂ Reduction to Formate. *Angew. Chem. Int. Ed.* **2024**, *63*, e202316640. [[CrossRef](#)] [[PubMed](#)]
42. Ma, Y.; Jia, Y.; Wang, L.; Yang, M.; Bi, Y.; Qi, Y. Efficient Charge Separation between Bi and Bi⁰-Bi₂MoO₆ for Photoelectrochemical Properties. *Chem. Eur. J.* **2016**, *22*, 5844–5848. [[CrossRef](#)] [[PubMed](#)]
43. Ma, T.; Yang, C.; Guo, L.; Soomro, R.A.; Wang, D.; Xu, B.; Fu, F. Refining electronic properties of Bi₂MoO₆ by In-doping for boosting overall nitrogen fixation via relay catalysis. *Appl. Catal. B Environ.* **2023**, *330*, 122643. [[CrossRef](#)]
44. Yu, B.; Wu, Y.; Meng, F.; Wang, Q.; Jia, X.; Wasim Khan, M.; Huang, C.; Zhang, S.; Yang, L.; Wu, H. Formation of hierarchical Bi₂MoO₆/In₂S₃ S-scheme heterojunction with rich oxygen vacancies for boosting photocatalytic CO₂ reduction. *Chem. Eng. J.* **2022**, *429*, 132456. [[CrossRef](#)]
45. Li, X.; Dong, Q.; Li, F.; Zhu, Q.; Tian, Q.; Tian, L.; Zhu, Y.; Pan, B.; Padervand, M.; Wang, C. Defective Bi@BiOBr/C microrods derived from Bi-MOF for efficient photocatalytic NO abatement: Directional regulation of interfacial charge transfer via carbon-loading. *Appl. Catal. B-Environ. Energy* **2024**, *340*, 123238. [[CrossRef](#)]
46. Zhang, L.; Wang, Z.; Hu, C.; Shi, B. Enhanced photocatalytic performance by the synergy of Bi vacancies and Bi⁰ in Bi⁰-Bi₂MoO₆. *Appl. Catal. B-Environ.* **2019**, *257*, 117785. [[CrossRef](#)]
47. Zhu, Q.; Hailili, R.; Xin, Y.; Zhou, Y.; Huang, Y.; Pang, X.; Zhang, K.; Robertson, P.K.J.; Bahnemann, D.W.; Wang, C. Efficient full spectrum responsive photocatalytic NO conversion at Bi₂Ti₂O₇: Co-effect of plasmonic Bi and oxygen vacancies. *Appl. Catal. B Environ.* **2022**, *319*, 121888. [[CrossRef](#)]
48. Zhao, X.; Li, J.; Kong, X.; Li, C.; Lin, B.; Dong, F.; Yang, G.; Shao, G.; Xue, C. Carbon Dots Mediated In Situ Confined Growth of Bi Clusters on g-C₃N₄ Nanomeshes for Boosting Plasma-Assisted Photoreduction of CO₂. *Small* **2022**, *18*, 202204154. [[CrossRef](#)]
49. Qin, D.; Song, S.; Liu, Y.; Wang, K.; Yang, B.; Zhang, S. Enhanced Electrochemical Nitrate-to-Ammonia Performance of Cobalt Oxide by Protic Ionic Liquid Modification. *Angew. Chem. Int. Ed.* **2023**, *62*, 202304935. [[CrossRef](#)]
50. Shipman, M.A.; Symes, M.D. Recent progress towards the electrosynthesis of ammonia from sustainable resources. *Catal. Today* **2017**, *286*, 57–68. [[CrossRef](#)]

51. Sun, Y.; Ji, H.; Sun, Y.; Zhang, G.; Zhou, H.; Cao, S.; Liu, S.; Zhang, L.; Li, W.; Zhu, X.; et al. Synergistic Effect of Oxygen Vacancy and High Porosity of Nano MIL-125(Ti) for Enhanced Photocatalytic Nitrogen Fixation. *Angew. Chem. Int. Ed.* **2023**, *63*, 202316973. [[CrossRef](#)] [[PubMed](#)]
52. Chen, X.; Zhang, X.; Li, Y.-H.; Qi, M.-Y.; Li, J.-Y.; Tang, Z.-R.; Zhou, Z.; Xu, Y.-J. Transition metal doping BiOBr nanosheets with oxygen vacancy and exposed {102} facets for visible light nitrogen fixation. *Appl. Catal. B Environ.* **2021**, *281*, 119516. [[CrossRef](#)]
53. Vesali-Kermani, E.; Habibi-Yangjeh, A.; Diarmand-Khalilabad, H.; Ghosh, S. Nitrogen photofixation ability of g-C₃N₄ nanosheets/Bi₂MoO₆ heterojunction photocatalyst under visible-light illumination. *J. Colloid Interface Sci.* **2020**, *563*, 81–91. [[CrossRef](#)] [[PubMed](#)]
54. Sharma, M.; Kumar, A.; Gill, D.; Jaiswal, S.; Patra, A.; Bhattacharya, S.; Krishnan, V. Boosting Photocatalytic Nitrogen Fixation via Nanoarchitectonics Using Oxygen Vacancy Regulation in W-Doped Bi₂MoO₆ Nanosheets. *ACS Appl. Mater. Interfaces* **2023**, *15*, 55765–55778. [[CrossRef](#)] [[PubMed](#)]
55. Liu, Z.; Luo, M.; Cao, Y.; Meng, L.; Yang, Y.; Li, X. Tuning the electronic properties of Bi₂MoO₆ by S-doping to boost efficient photocatalytic nitrogen fixation reactions. *J. Catal.* **2024**, *430*, 115347. [[CrossRef](#)]
56. Zhu, C.; Zhang, L.; Cui, L.; Zhang, Z.; Li, R.; Wang, Y.; Wang, Y.; Fan, C.; Yu, Z.; Liu, J. Fe-Bi dual sites regulation of Bi₂O_{2.33} nanosheets to promote photocatalytic nitrogen fixation activity. *J. Colloid Interface Sci.* **2024**, *661*, 46–58. [[CrossRef](#)] [[PubMed](#)]
57. Wang, H.; Chen, Z.; Shang, Y.; Lv, C.; Zhang, X.; Li, F.; Huang, Q.; Liu, X.; Liu, W.; Zhao, L.; et al. Boosting Carrier Separation on a BiOBr/Bi₄O₅Br₂ Direct Z-Scheme Heterojunction for Superior Photocatalytic Nitrogen Fixation. *ACS Catal.* **2024**, *14*, 5779–5787. [[CrossRef](#)]
58. Huang, X.; Du, R.; Zhang, Y.; Ren, J.; Yang, Q.; Wang, K.; Ni, Y.; Yao, Y.; Ali Soomro, R.; Guo, L.; et al. Modulating charge oriented accumulation via interfacial chemical-bond on In₂O₃/Bi₂MoO₆ heterostructures for photocatalytic nitrogen fixation. *J. Colloid Interface Sci.* **2024**, *664*, 33–44. [[CrossRef](#)]
59. Dong, Q.; Li, X.; Sun, J.; Zhu, Y.; Liang, X.; Ren, H.; Labidi, A.; Wang, D.; Li, F.; Wang, C. Regulating concentration of surface oxygen vacancies in Bi₂MoO₆/Bi-MOF for boosting photocatalytic ammonia synthesis. *J. Catal.* **2024**, *433*, 115489. [[CrossRef](#)]
60. Zhang, G.; Yuan, X.; Xie, B.; Meng, Y.; Ni, Z.; Xia, S. S vacancies act as a bridge to promote electron injection from Z-scheme heterojunction to nitrogen molecule for photocatalytic ammonia synthesis. *Chem. Eng. J.* **2022**, *433*, 133670. [[CrossRef](#)]
61. Li, H.; Zhang, J.; Deng, X.; Wang, Y.; Meng, G.; Liu, R.; Huang, J.; Tu, M.; Xu, C.; Peng, Y.; et al. Structure and Defect Engineering Synergistically Boost High Solar-to-Chemical Conversion Efficiency of Cerium oxide/Au Hollow Nanomushrooms for Nitrogen Photofixation. *Angew. Chem.-Int. Ed.* **2024**, *63*, e202316384. [[CrossRef](#)] [[PubMed](#)]
62. Bian, X.; Zhao, Y.; Zhang, S.; Li, D.; Shi, R.; Zhou, C.; Wu, L.-Z.; Zhang, T. Enhancing the Supply of Activated Hydrogen to Promote Photocatalytic Nitrogen Fixation. *ACS Mater. Lett.* **2021**, *3*, 1521–1527. [[CrossRef](#)]
63. Gao, X.; Shang, Y.; Liu, L.; Gao, K. Ag plasmon resonance promoted 2D AgBr-δ-Bi₂O₃ nanosheets with enhanced photocatalytic ability. *J. Alloys Compd.* **2019**, *803*, 565–575. [[CrossRef](#)]
64. Yang, J.; Guo, Y.; Jiang, R.; Qin, F.; Zhang, H.; Lu, W.; Wang, J.; Yu, J.C. High-Efficiency “Working-in-Tandem” Nitrogen Photofixation Achieved by Assembling Plasmonic Gold Nanocrystals on Ultrathin Titania Nanosheets. *J. Am. Chem. Soc.* **2018**, *140*, 8497–8508. [[CrossRef](#)]
65. Jia, H.; Du, A.; Zhang, H.; Yang, J.; Jiang, R.; Wang, J.; Zhang, C.-y. Site-Selective Growth of Crystalline Ceria with Oxygen Vacancies on Gold Nanocrystals for Near-Infrared Nitrogen Photofixation. *J. Am. Chem. Soc.* **2019**, *141*, 5083–5086. [[CrossRef](#)]

Disclaimer/Publisher’s Note: The statements, opinions and data contained in all publications are solely those of the individual author(s) and contributor(s) and not of MDPI and/or the editor(s). MDPI and/or the editor(s) disclaim responsibility for any injury to people or property resulting from any ideas, methods, instructions or products referred to in the content.